

# Rapid Exploration of a 32.5M Compound Chemical Space with Active Learning to Discover Density Functional Approximation Insensitive and Synthetically Accessible Transitional Metal Chromophores

Chenru Duan<sup>1,2</sup>, Aditya Nandy<sup>1,2</sup>, Gianmarco Terrones<sup>1</sup>, David W. Kastner<sup>1,3</sup>, and Heather J. Kulik<sup>1,2</sup>

<sup>1</sup>Department of Chemical Engineering, Massachusetts Institute of Technology, Cambridge, MA 02139

<sup>2</sup>Department of Chemistry, Massachusetts Institute of Technology, Cambridge, MA 02139

<sup>3</sup>Department of Biological Engineering, Massachusetts Institute of Technology, Cambridge, MA 02139

Two outstanding challenges for machine learning (ML)-accelerated chemical discovery are the synthesizability of candidate molecules or materials and the fidelity of the data used in ML model training. To address the first challenge, we construct a hypothetical design space of 32.5M transition metal complexes (TMCs), in which all of the constituent fragments (i.e., metals and ligands) and ligand symmetries are synthetically accessible. To address the second challenge, we search for consensus in predictions among 23 density functional approximations across multiple rungs of “Jacob’s ladder”. To accelerate the screening of these 32.5M TMCs, we use efficient global optimization to sample candidate low-spin chromophores that simultaneously have low absorption energies and low static correlation. Despite the scarcity (i.e., < 0.01%) of potential chromophores in this large chemical space, we identify transition metal chromophores with high likelihood (i.e., > 10%) as the ML models improve during active learning. This represents a 1,000 fold acceleration in discovery corresponding to discoveries in days instead of years. Analyses of candidate chromophores reveal a preference for Co(III) and large, strong-field ligands with more bond saturation. We compute the absorption spectra of promising chromophores on the Pareto front by time-dependent density functional theory calculations and verify that 2/3 of them have desired excited state properties. Although these complexes have never been experimentally explored, their constituent ligands demonstrated interesting optical properties in literature, exemplifying the effectiveness of our construction of realistic TMC design space and active learning approach.

## Introduction

Virtual high throughput screening (VHTS)<sup>1-12</sup> and machine learning (ML)<sup>13-19</sup> have shown great promise and have started to address combinatorial challenges in accelerating the design of functional molecules and materials. Here, VHTS is used to generate a large data set of materials or molecules are studied with density functional theory (DFT) to develop structure-property relationships.<sup>7, 20-26</sup> Then either supervised learning (i.e., forward) models<sup>13-16, 27</sup> are trained to screen through a large pre-constructed design space or generative (i.e., inverse) models<sup>28-29</sup> are applied to obtain candidate molecules with targeted properties. A naïve “one shot” approach is usually too data greedy and may suffer from the stochasticity of the sampling process. Therefore, active learning with Bayesian optimization<sup>30-32</sup> has been recognized as an attractive paradigm for balancing data acquisition in ML model training (i.e., exploration) and ML-model-based prediction (i.e., exploitation) for chemical discovery<sup>33-36</sup>, demonstrating a 500-fold acceleration<sup>37</sup> compared to random search.

Despite the success of this active learning workflow in many applications, there remain significant challenges that prevent experimental realization of the candidate molecules yielded from computational workflows. First, although one can add explicit constraints on ML models, it is still difficult to guarantee that the lead molecules selected by the supervised learning model or created by the generative model are synthesizable<sup>38-40</sup>. Second, the DFT outcome depends on the density functional approximation (DFA) choice. A DFA that works well on certain systems may fail prominently on other systems due to the approximations made in the exchange-correlation functional<sup>4, 41-42</sup>. Combined with the single-DFA approach widely used in VHTS, DFA choices can lead to large biases in the data sets generated, which in turn biases ML models and eventually introduces uncertainties to candidate molecules proposed by the models<sup>43</sup>.

These two challenges are particularly outstanding in the design of functional transition metal complexes (TMCs). There, the synthesizability problem becomes multiplicative<sup>44</sup> (i.e., all ligands comprising a TMC need to be synthesizable), and the electronic structure of a TMC is sometimes dominated by static correlation<sup>45</sup> that would make DFT error-prone and predictions highly sensitive to DFA choice. Transition metal chromophores are a typical design target because they play an important role in many chemical and biological processes ranging from natural light harvesting<sup>46-48</sup>, light-emitting technologies<sup>49</sup> to photocatalysis<sup>50-51</sup>. Due to the delicate interplay<sup>52-53</sup> required to tune complex properties, it is challenging to use a standard Edisonian approach<sup>54</sup> to simultaneously alter metal-ligand interactions, ligand field strength, electron donating/withdrawing effects, and the relative energetic positioning between the ground and excited state potential energy surfaces. A notable exception is a recent work<sup>55</sup> that utilized high throughput experiments to identify heteroleptic Ir(III)-based chromophores. Nevertheless, to facilitate scalable materials design, transition metal chromophores made with  $3d$  earth-abundant metals with  $d^6$  electron configuration are preferred relative to their state-of-the-art  $4d$  and  $5d$  metals (e.g. Ru(II) and Ir(III)) analogs<sup>52-53, 56</sup>.

In this work, we applied efficient global optimization<sup>57</sup> (EGO) to discover  $3d^6$  Fe(II)/Co(III) transition metal chromophores in a design space with 32.5M TMCs. We addressed the outstanding challenge of synthesizability of candidate chromophores by carefully crafting the design space with constraints using synthetically accessible fragments and ligand symmetries in Cambridge Structural Database (CSD). We avoid bias from DFA choice by applying a DFA-consensus approach<sup>43</sup> that considers property evaluation as an ensemble of predictions from 23 DFAs that span multiple rungs of “Jacob’s ladder”<sup>58</sup>. Our active learning approach successfully identifies promising transition metal chromophores and is estimated to exhibit a 1,000-fold acceleration

compared to the random sampling. We reveal that Co(III) complexes with large, strong-field ligands with more saturated bonds are preferred as candidate transition metal chromophores. By invoking Hammett tuning effects<sup>59</sup> and introducing functionalization on compounds, we further extended the Pareto front of the potential transition metal chromophores and verified our most promising candidates with time-dependent DFT (TDDFT) calculations.

## Results and Discussion

**Design space.** We construct and explore a hypothetical design space of TMCs where all the constituent fragments (i.e., metals and ligands) are synthetically accessible (Figure 1). We further constrain the TMCs in the space to contain three bidentate ligands (e.g. Fe(II)(bpy)<sub>3</sub>) and restrict ourselves to *d*<sup>6</sup> Fe(II) or Co(III) metal centers, based on the precedent of this coordination type corresponding to efficient chromophores. We limit the number of unique ligands to two in a TMC to promote the likelihood of synthesizability. We started with 5,173 CSD ligands that we curated in previous work<sup>60</sup>, including by assigning the charge states of the ligands. From this set, we selected bidentate ligands that contain common elements (i.e., H, B, C, N, O, F, Si, P, S, Cl, Br, and I) and  $\leq 25$  heavy (i.e., non-hydrogen) atoms, leaving a set of 812 ligands (Supporting Information). Combined with either Fe(II) or Co(III), the constraint of forming a complex with up to two unique bidentate ligands in an octahedral complex with three bidentate ligands produces  $2 \times 812 = 1,624$  homoleptic and  $2 \times 812 \times 811 = 1,317,064$  heteroleptic TMCs. We refer to these 1.3M TMCs as the “base complexes”. Hammett tuning is a commonly adopted strategy in experiments to fine tune the electronic properties of a complex by adding electron-donating or electron-withdrawing functional groups on conjugated rings. Here, we consider three distinct functionalization positions and ten functional groups, expanding the final design space to 32.5M

functionalized TMCs, which we refer to as the “functionalized complex space” (Figure 1, see details at Section *Exploring the functionalized design space*).

**Active learning procedure and design criteria.** In transition metal chromophores, the photo-excited state should have a lifetime that is sufficiently long, such that the resulting chemical potential can be redirected before it is lost to unproductive competing pathways. Correspondingly, it is advantageous to have the photo-excited electron populated in a long-lived metal-ligand charge transfer (MLCT) state and avoid low-lying metal centered (MC) states that deactivate electron transfer from the expected photo-excited state. Therefore, we target complexes with low-spin (LS) ground states to increase the likelihood for the presence of MLCT state and to destabilize the MC state<sup>53</sup>. We also need target complexes to have weak multi-reference (MR) character to avoid low-lying states and reduce the likelihood of inaccuracy in DFT results, which is may be efficiently measured from fractional occupation number DFT as the contribution from nondynamical correlation<sup>61-62</sup> (i.e.,  $r_{\text{ND}}$ <sup>63</sup>, see *Methods*). In addition, the absorption energy should match the wavelengths of the visible spectrum of sunlight, ranging from 1.5 eV (825 nm) and 3.5 eV (350 nm). Since the HOMO-LUMO gap is extremely sensitive to DFA choice, the absorption energy is usually estimated by  $\Delta$ -SCF calculations<sup>64</sup>, which are more robust (see *Methods*).

We use EGO with a 2D probability of improvement (P[I]) criterion to sample TMCs with LS ground state in a target zone of [1.5 eV, 3.5 eV] for  $\Delta$ -SCF gap and [0, 0.307] for  $r_{\text{ND}}$  as candidate transition metal chromophores (Figure 1). The cutoff of 0.307 for  $r_{\text{ND}}$  was chosen from our previous work<sup>65</sup> as a distinguishing cutoff for TMCs with weak vs. strong MR character . For EGO, we largely followed the established protocols from our previous work<sup>36-37</sup>: complexes in

each new generation were selected by  $k$ -medoids sampling over the full design space. We then used DFT to evaluate the  $\Delta$ -SCF gap,  $r_{\text{ND}}$ , and ground spin state of these complexes. After combining the new data with data from previous generations, we retrained our ML models. Lastly, we used the updated ML models to evaluate the ground spin state and 2D P[I] of the complexes. We selected the top 2,000 TMCs for  $k$ -medoids sampling to obtain the 200 complexes for DFT simulation in the next generation. Importantly, since both the ground state assignment and  $\Delta$ -SCF gap are still sensitive to DFA choice, we adopt our DFA consensus procedure<sup>43</sup>, where we considered an ensemble of 23 DFAs that cover the broad spectrum of the “Jacob’s ladder” and demonstrated the improved correspondence to experimental observations, to increase the robustness of our lead candidate chromophores (Supporting Information Figures S1-S3). Specifically, we only retain complexes when a majority of DFAs (i.e., 70% or > 16 of 23) predict the complex to have a LS ground state (Supporting Information Table S1). During the evaluation of 2D P[I], we consider ML models trained on 23 DFAs separately, from which the  $\Delta$ -SCF gap and its corresponding model uncertainty are estimated. Only the averages of  $\Delta$ -SCF gap and 2D P[I] among 23 DFAs are used to rank and sample TMCs in the next generation.

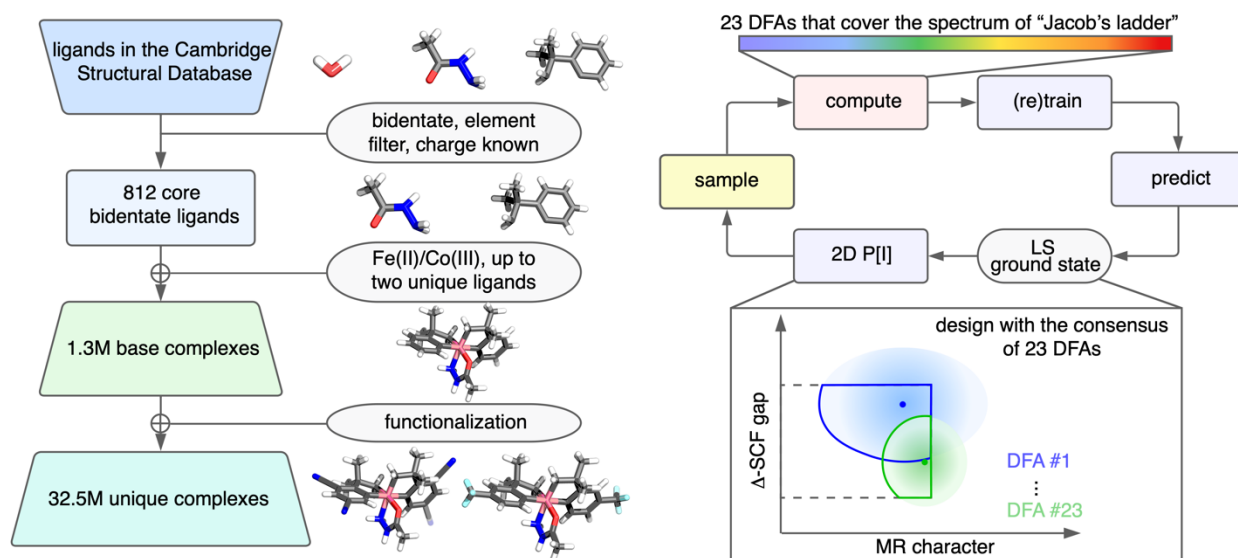


**Figure 1.** (left) Hierarchical assembly of the 32.5M complex design space for transition metal chromophore design. All ligands in the CSD are first filtered to only retain bidentate ligands with common elements and  $\leq 25$  heavy atoms, and known charge. These 812 bidentate ligands are paired with either Fe(II) or Co(III), under the constraint that each complex has  $\leq 2$  unique ligand types, to form a design space of 1.3M base complexes. Lastly, these complexes are expanded to the full design space of 32.5M complexes with functionalization on the coordinating rings with a series of electron-donating or electron-withdrawing functional groups. (right) Active learning for discovering DFA-consensus-designed transition metal chromophores. DFT simulations are performed with 23 DFAs that span multiple rungs of “Jacob’s ladder”, which are used to iteratively train ML models. These ML models are applied to predict the ground spin state and  $\Delta$ -SCF gap of complexes for 23 DFAs, and the MR character and their corresponding uncertainties. These quantities are used to select complexes with LS ground state and to evaluate the 2D P[I] of the design space to sample candidate complexes to compute in the next generation. The inset is an illustration of the ML prediction (solid dot), uncertainty (shaded area), and effective 2D P[I] area (solid outline) for multiple DFAs (blue and green) with respect to a target zone (rectangle with dashed lines).

**Active learning on the 1.3M base complexes.** We observe a strong negative linear correlation between  $\Delta$ -SCF gap and  $r_{\text{ND}}$  for the 2,000 TMCs sampled in gen-0, which introduces difficulties for identifying candidates with simultaneously low  $\Delta$ -SCF gap and  $r_{\text{ND}}$  (Figure 2). This negative linear correlation exists because a small  $\Delta$ -SCF gap generally suggests the existence of low-lying excited states, which would lead to high  $r_{\text{ND}}$  as MR character arises from near degenerate occupied and virtual orbitals. In addition, we find that LS complexes often have stronger MR character, and thus higher  $r_{\text{ND}}$ , relative to their HS counterparts since they can access more configuration state functions<sup>65</sup> (Supporting Information Figure S4). The nature of this multiple objective search for transition metal chromophores suggests that TMCs that can fulfill all our design requirements will be scarce. Indeed, for the 2,000 TMCs selected from  $k$ -medoids sampling in gen-0, no complex with an LS ground state matches our target criteria with desirably low  $\Delta$ -SCF gap and  $r_{\text{ND}}$  (Figure 2). If we assume the probability of a TMC residing in the target zone is as low as 0.01%, we still have 20% chance of getting at least one TMC in the target zone with 2,000 random samples. Our

ML models trained on gen-0 data also give a similarly conservative estimate that only 0.018% of TMCs have  $> 1/3$  2D P[I] to fulfill our design criteria (Figure 2).

Despite the scarcity of promising transition metal chromophores, we successfully increase the population of lead TMCs in the target zone through active learning. The distributions of the sampled points in gen-1 to gen-3 clearly shift towards the target zone, despite the negative linear correlation between  $\Delta$ -SCF gap and  $r_{\text{ND}}$  (Figure 2). Although only 200 complexes were sampled at each subsequent generation after an initial sampling of 2,000 complexes, we still discover numerous TMCs in the target zone after their DFT properties are computed. This enrichment is greatest in gen-2, where we identify 14 new TMCs, leading to a rather high (i.e., 7%) lead conversion rate (i.e., number of leads over number of samples). A conservative estimate using the binomial distribution shows that one would need to sample 200,000 TMCs randomly in the base complex space to produce 14 lead complexes, demonstrating a 1,000-fold acceleration of our active learning approach compared to random sampling. In addition, the ML models improve systematically as active learning proceeds from gen-0 to gen-3, as exemplified by reduction in relative MAEs of predicting the DFT properties on the set-aside test data with increasing model generation (Figure 2, Supporting Information Figure S5, see *Methods*).

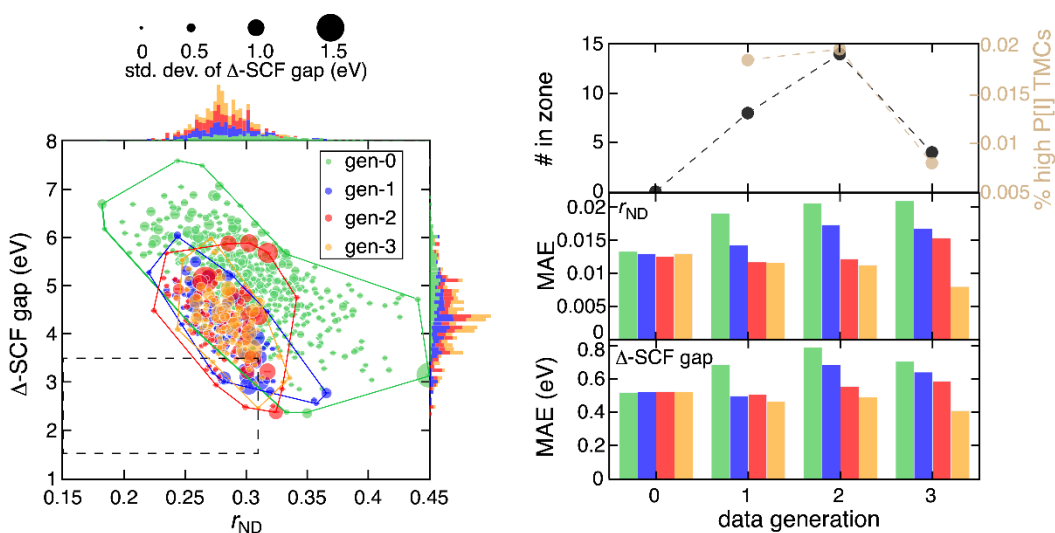


**Figure 2.** (left) DFT computed  $\Delta$ -SCF gap vs.  $r_{\text{ND}}$  for base complexes in gen-0 to gen-3. For each complex, the average of  $\Delta$ -SCF gap over all DFAs is shown as a circle sized by the corresponding std. dev. of  $\Delta$ -SCF gaps over all DFAs. The range of values sampled in each generation is indicated by a convex hull. The target zone is shown as a rectangle with dashed lines. Normalized stacked marginal histograms for  $\Delta$ -SCF gap and  $r_{\text{ND}}$  are also shown. (right) The number of complexes in the target zone (black) and the percentage of the design space that has a 2D  $P[\text{I}] > 1/3$  (tan) at each generation (top). The 2D  $P[\text{I}]$  at gen-0 is not available as the ML models have only been trained after gen-0. MAE for  $r_{\text{ND}}$  (middle) and  $\Delta$ -SCF gap (bottom) from gen-0 to gen-3. At each generation, the ML models are trained on the combined training set of all previous generations and are tested on the set-aside test set of each generation separately. For example, the gen-2 model (blue bars) was trained on the combined training set of gen-0, gen-1, and gen-2 data. Generations are colored as follows throughout: green for gen-0, blue for gen-1, red for gen-2, and orange for gen-3. Gen-0 represents a  $k$ -medoids sampling of the 1.3M base TMC space.

After three generations of active learning, both the number of TMCs landing in the target zone (i.e., after computed by DFT) and the percentage of high 2D  $P[\text{I}]$  complexes decrease, indicating likely depletion of candidate base TMCs as well as the leveling off of ML model performance on the 1.3M base complexes. Therefore, we used the gen-3 models to screen through the base complex design space to reveal chemical trends for the 2,432 TMCs that have a high probability of residing in the target zone (i.e., 2D  $P[\text{I}] > 1/6$ ). From those high 2D  $P[\text{I}]$  complexes, we find that complexes with Co(III) and strong-field ligands (e.g. coordinating atom combinations of: CC, CN, NP, and PP) are significantly enriched (Figure 3). This likely occurs due to our

requirement of a LS ground state during the screening procedure (Figure 1). Since we prefer a small  $\Delta$ -SCF gap, the complexes that are favored by 2D P[I] tend to have large ligands, consistent with our previous observation that  $\Delta$ -SCF gap has a negative linear correlation with complex size<sup>65</sup> (Figure 3). Lastly, we find that complexes with high (i.e.,  $> 1/6$ ) 2D P[I] tend to consist of ligands that are more saturated, as measured by their increased inverse average bond order<sup>60</sup> (Figure 3). This trend can be understood by the fact that unsaturated ligands tend to contain higher MR character and the ligand additivity effects (i.e., properties of ligands accumulate in a TMC)<sup>60</sup> (Supporting Information Figure S6). In general, we successfully learn from our ML models that a complex with Co(III) and large, strong-field, and relatively saturated ligands would have an increased chance of becoming a transition metal chromophore with desired properties.

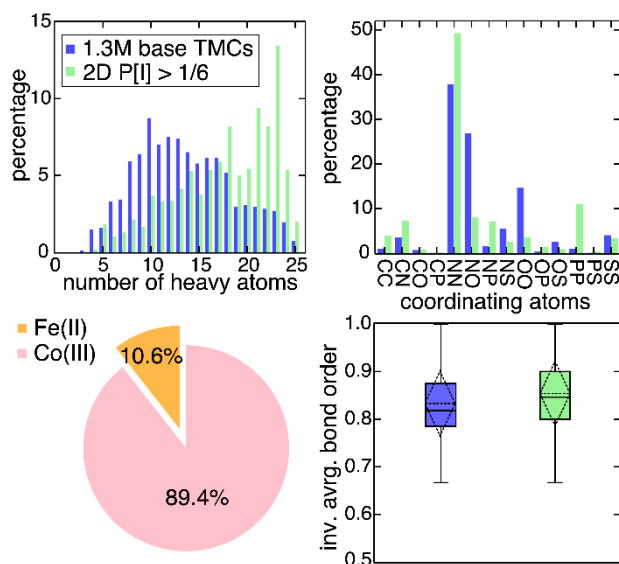


**Figure 3.** Comparison of property distributions of the 2,432 complexes with 2D PI  $> 1/6$  evaluated by gen-3 ML models (green) and the 1.3M base complexes (blue). Bar plots for the average number of heavy atoms in the ligands involved in the 2,432 complexes (top left) and their coordinating atom types (top right), a pie chart for the core metal (orange for Fe(II) and pink for Co(III), bottom left), and a box plot for inverse average (inv. avrg.) bond order for the ligands (bottom right). For each box, the median is shown as a horizontal solid line, the mean and std. dev. are shown as a dashed diamond, and the two extrema are shown by the vertical bar.

**Exploring the functionalized design space.** Hammett tuning, i.e., functionalization on conjugated rings, is a common procedure applied in experiments to fine tune the electronic properties of a TMC without dramatically scarifying its synthesizability.<sup>66-67</sup> We considered three possible functionalizable positions, categorized by the bond depth ( $d$ ) of the H atom on a ring with respect to the metal (Figure 4). For a six-membered ring,  $d=3, 4,$  or  $5$  corresponds to the ortho, meta, and para positions, respectively. For a five-membered ring, only  $d=3$  or  $4$  is feasible. We consider a wide range of 10 electron-donating or electron-withdrawing functional groups (Figure 4). To retain good likelihood of synthesizability, we constrain the *in silico* functionalization procedure to consist of one unique functionalizable position and one unique functional group for a TMC and disallow any combinations with multiple functionalizable positions or functional groups. Despite this constraint, the base design space will roughly be expanded by a factor of 25 after accounting for rings that are not functionalizable, leading to 32.5M TMCs (Figure 1). The effect of Hammett tuning, however, will not be large enough to move all 1.3M base complexes into the target zone. On a representative Co(III) complex that resides in the target zone, we find that Hammett tuning can roughly tune the  $\Delta$ -SCF gap by 1.0 eV and  $r_{\text{ND}}$  by 0.04 (Figure 4). Therefore, we use the gen-3 ML models to screen through the 1.3M base complexes and only keep TMCs with predicted  $\Delta$ -SCF gap  $< 4.5$  eV and  $r_{\text{ND}} < 0.35$  as candidates for Hammett tuning. These promising 30.1k base complexes lead to a design space of 0.8M functionalized TMCs for further exploration.

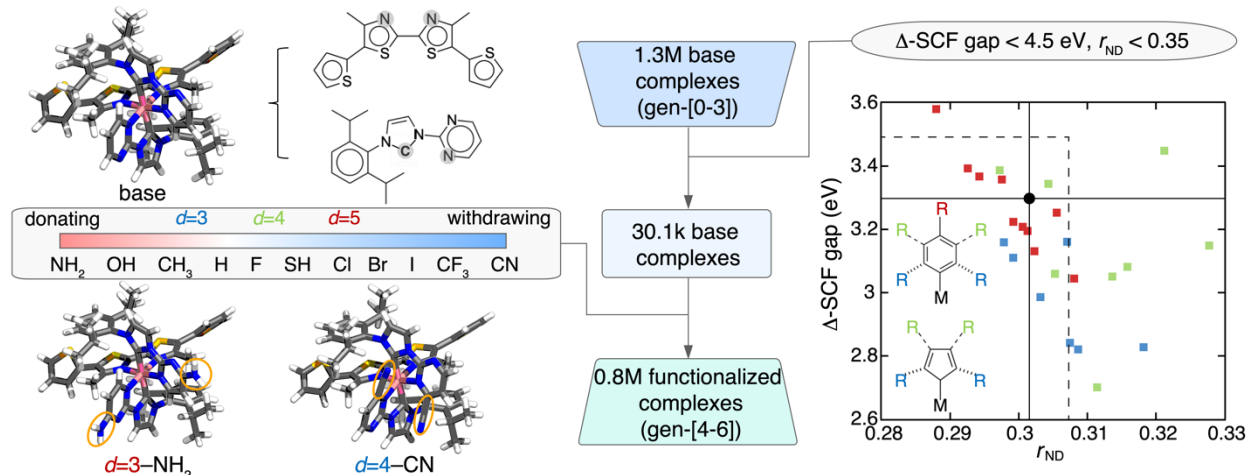


**Figure 4.** Procedure for constructing the functionalized TMC design space. (middle) The 1.3M base complexes used in gen-0 to gen-3 are first filtered down to 30.1k base complexes that are predicted to have a low-spin GS, an average  $\Delta$ -SCF gap < 4.5 eV, and  $r_{ND}$  < 0.35, based on gen-3 ML models. These complexes are then functionalized on the coordinating rings with a chosen position (i.e.,  $d=3$ , 4, or 5) and functional group, enlarging the design space to 0.8M functionalized TMCs to be used in gen-4 to gen-6. (left) Example of functionalizing the base complex Co(III)(C<sub>19</sub>H<sub>22</sub>N<sub>4</sub>)<sub>2</sub>(C<sub>16</sub>H<sub>12</sub>N<sub>2</sub>S<sub>4</sub>). The base complex and corresponding ligands are shown at the top, where the coordinating atoms are shaded in gray. The functional groups used to perform Hammett tuning are shown in the middle. The two functionalized complexes (left with CN at the  $d=3$  position and right with NH<sub>2</sub> at the  $d=4$  position) are shown at the bottom. (right) Average  $\Delta$ -SCF gap vs.  $r_{ND}$  for functionalized Co(III)(C<sub>19</sub>H<sub>22</sub>N<sub>4</sub>)<sub>2</sub>(C<sub>16</sub>H<sub>12</sub>N<sub>2</sub>S<sub>4</sub>) at all possible positions (blue for  $d=3$ , green for  $d=4$ , and red for  $d=5$ ) and functional groups. The target zone is shown as a rectangle with dashed lines. The predicted properties of Co(III)(C<sub>19</sub>H<sub>22</sub>N<sub>4</sub>)<sub>2</sub>(C<sub>16</sub>H<sub>12</sub>N<sub>2</sub>S<sub>4</sub>) are shown as a black circle intersected with solid lines. The insets show the rule of functionalizing a six-membered and five-membered ring, respectively.

Since we have created a new design space with functionalized complexes that our ML models have not seen before, we expect that the 2D P[I] computed based on the trained model predictions and uncertainties would not be able to directly guide the exploration of candidate chromophores. Therefore, we repeated the  $k$ -medoids sampling that we performed in gen-0 but this time limited to the new 0.8M functionalized design space, selecting a set of 200 complexes. Indeed, we find that the gen-3 models have significantly higher errors on the predictions of the  $k$ -medoids sampled gen-4 data (Figure 5). However, the ML models improve quickly after retraining on the functionalized complexes in gen-4. Therefore, we expect the 2D P[I] to regain its predictive

power and proceeded two generations of active learning using 2D P[I] criteria. During these two generations, the ML models achieve MAEs that are comparable to those on the base complexes (Figure 5). Since we have already isolated this more promising functionalized TMC space, both the number of TMCs landing in the target zone and the percentage of high 2D P[I] complexes increase relative to the previous three generations (Figure 5). At both gen-5 and gen-6, 19 (i.e., 10%) of the sampled functionalized TMCs are verified as candidate transition metal chromophores by DFA consensus. This number greatly surpasses the average (i.e., 6) and the maximum (i.e., 14) in the previous generations. More importantly, the sampled functionalized complexes in gen-5 and gen-6 further expand the convex hull in the 2D property space, with their distributions shifted towards the target zone. This observation showcases the effectiveness of our strategy for using Hammett tuning to further enrich a pool of candidate chromophores and improve their electronic properties.

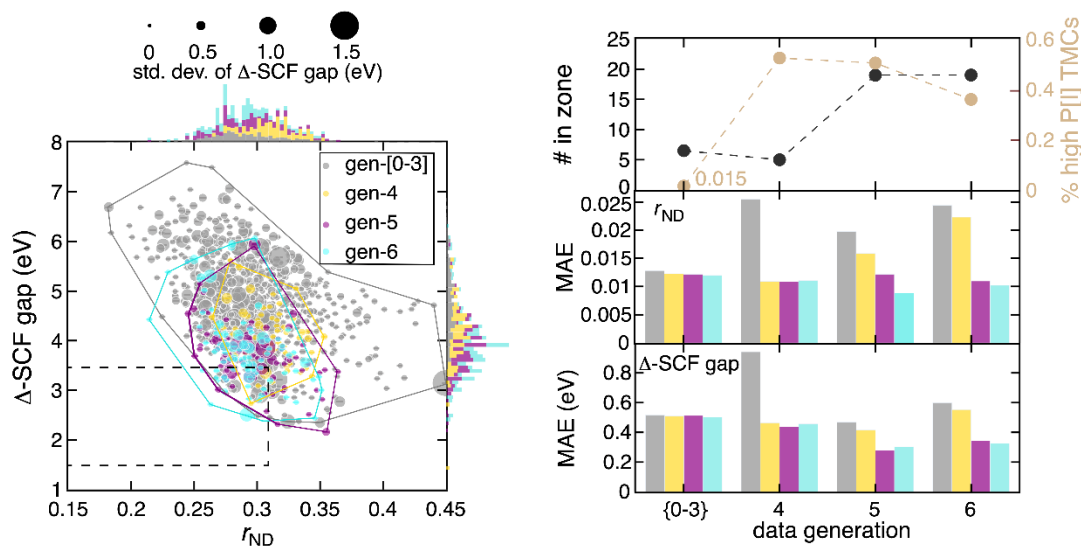


**Figure 5.** (left) DFT-computed  $\Delta$ -SCF gap vs.  $r_{ND}$  for functionalized complexes from gen-4 to gen-6 (yellow for gen-4, purple for gen-5, and cyan for gen-6). The base complexes in gen-0 to gen-3 are combined as gen-[0-3] (gray). For each complex, the average of  $\Delta$ -SCF gap of all DFAs is shown as a circle scaled by the corresponding std. dev. of  $\Delta$ -SCF gaps. The range of values sampled in each generation is indicated by a convex hull. The target zone is shown as a rectangle with dashed lines. Normalized stacked marginal histograms for  $\Delta$ -SCF gap and  $r_{ND}$  are also shown.

(right) The number of complexes in the target zone (black) and the percentage of the design space that has a 2D  $P[I] > 1/3$  (tan) at each generation (top), with the average shown for the combined gen-[0-3]. MAE for  $r_{\text{ND}}$  (middle) and  $\Delta$ -SCF gap (down) at each generation. At each generation, the ML models are trained on the combined training set of all previous generations and are tested on the set-aside test set of each generation separately. For the combined gen-[0-3], the MAEs are evaluated on the combined set-aside test sets from gen-0 to gen-3 using the gen-3 ML models. Gen-4 represents a  $k$ -medoids sampling of 200 TMCs on the 0.8M functionalized TMC space.

To further verify that complexes discovered through the active learning process have desired excited state properties as candidate transition metal chromophores, we computed the excited state properties with TDDFT of lead light harvesting complexes on the Pareto front from all seven generations (see *Methods*). Using this approach, we verified that six out of nine of our Pareto front complexes have desired excited state transition energy  $< 3.5$  eV, where the electron transfer process involves a MLCT state (Figure 6). This observation is surprising since we do not explicitly set design objectives that involve explicit excited state calculations of our complexes during the active learning. Still, we achieve high likelihood (i.e., 67%) for obtaining lead complexes with promising excited state properties by carefully crafting the ground-state design objectives and using DFA consensus. The remaining three complexes have excited states with energy  $< 3.5$  eV but are “dark” states (i.e., with small oscillator strengths), which cannot be foreseen by the ground state calculations that we performed during the active learning procedure (Supporting Information Table S2).

In addition, we find that functionalization (i.e., Hammett tuning) indeed pushes the base complexes to the Pareto front by fine-tuning their electronic properties. For example, the  $d=3$   $\text{CH}_3$  functionalization of the base complex  $\text{Co(III)(N}_2\text{C}_{16}\text{H}_{12}\text{S}_4\text{)(N}_4\text{C}_{18}\text{H}_{16}\text{)}_2$  ( $\Delta$ -SCF gap=2.83 eV,  $r_{\text{ND}}=0.300$ ) leads to complex **F** ( $\Delta$ -SCF gap=2.39 eV,  $r_{\text{ND}}=0.305$ ), which lies on the Pareto front compared to other base complexes sampled in the active learning process (Figure 6, Supporting

Information Table S3). Since all the bidentate ligands considered are synthetically accessible, we propose these complexes as promising candidates for experimental verification. Moreover, although complexes **A-F** are not in the CSD, they all contain ligands present in other synthesized compounds that have demonstrated photo-induced properties (Supporting Information Table S4). For example, despite the fact that complex **F** has not been characterized experimentally, one of its constituent ligands (i.e., 4',5'-diaz-9'-[4,5-bis(methylthio)-1,3-dithiol-2-ylidene]fluorene) has been studied<sup>68</sup> for its interesting nonlinear optical properties in Co, Cu, and Cd complexes (Figure 6). These observations showcase the power of our strategy for identifying experimentally relevant candidate transition metal chromophores that were potentially missed by previous experimental exploration due to the combinatorial challenges in chemical discovery.

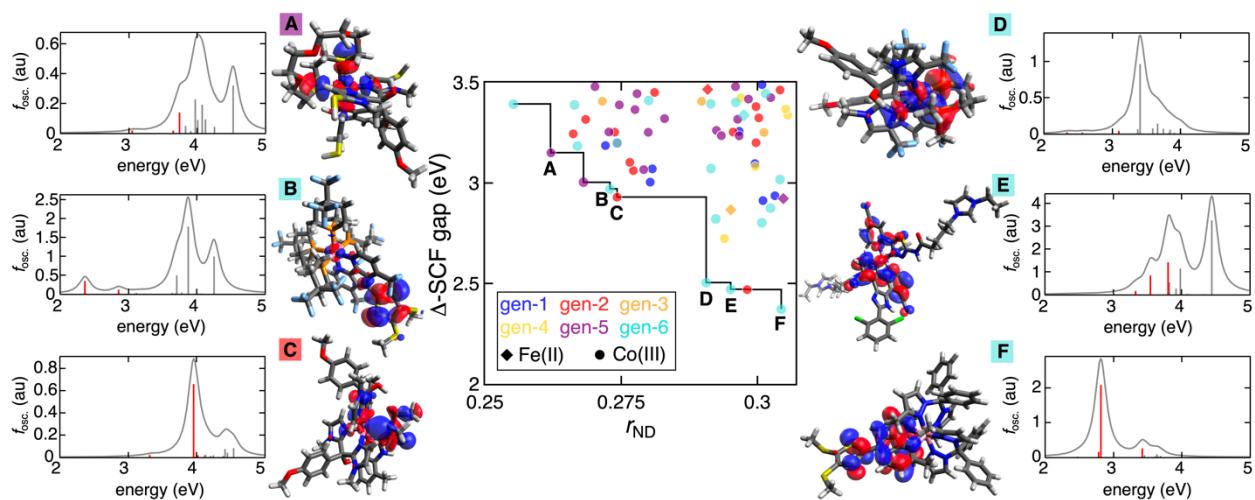


**Figure 6.** 69 TMCs sampled through the active learning process that have a LS ground state and land in the target zone computed by DFT, colored by generation and with unique symbols for each metal center (as indicated in the inset legend). The Pareto front is indicated by the black solid lines. Six out of nine TMCs on the Pareto front are verified to have desired excited state properties (i.e., an excited state lower than 3.5 eV and MLCT character) by TDDFT calculations. These six complexes are indicated by the letters **A–F**, where the absorption spectra and the lowest energy transition orbital are shown. The lowest three absorption energies are colored by red for better visibility due to the large variance among the oscillator strengths for different transition states.

## Conclusions

We applied EGO with a 2D P[I] criteria to discover potential  $3d^6$  Fe(II)/Co(III) transition metal chromophores in a design space with 32.5M compounds that simultaneously fulfill three design objectives: LS ground state, a small  $\Delta$ -SCF gap, and weak MR character. We addressed the salient challenge of synthesizability for computationally designed functional molecules by constraining the design space construction of only using ligands that are synthetically accessible and symmetry classes that are easy to access in experiments. We further avoid common biases that arise from DFA choice in VHTS and ML-accelerated chemical discovery by applying a DFA-consensus approach that considers the property evaluations from 23 DFAs that span multiple rungs of “Jacob’s ladder”. This way, compounds discovered through this active learning workflow have higher likelihood to be synthesizable and higher fidelity (i.e., more robust against sensitivity to DFA choice).

Despite the scarcity of potential transition metal chromophores in our design space, judged by the fact that no compounds in the initial 2,000 samples land in our target objective zone, our active learning process gradually shifts the distributions of sampled compounds towards the target zone and successfully identifies many leads. A conservative estimate based on a binomial distribution demonstrates that our active learning approach achieves a 1,000-fold acceleration relative to the random sampling, corresponding in practice to achieving new designs in one day instead of three years. With our ML models, we revealed that Co(III) complex with large, strong-field, and relatively saturated ligands are preferred as candidate transition metal chromophores. To fine-tune their electronic properties, we further introduced Hammett tuning by functionalization for base complexes, which further extended the Pareto front of the potential transition metal chromophores. Lastly, we performed TDDFT calculations on the nine most promising leads on

the Pareto front. We found six of the nine compounds demonstrate desired excited state properties with MLCT states and contain ligands that have been previously studied experimentally due to their interesting optical properties. We expect our strategy for design space construction and DFA-consensus enhanced active learning workflow to be broadly useful in discovering candidate molecules and materials that are more synthesizable and computationally robust in transition metal chemical spaces.

## Methods

**DFT calculation details.** All initial geometries were generated using molSimplify<sup>69-70</sup>, where initial ligand geometries were derived from the crystal structures of transition metal complexes containing the ligands (Supporting Information). DFT geometry optimizations were carried out using TeraChem<sup>71</sup>, as automated by molSimplify<sup>69-70</sup> with a 24 h wall time per run up to five resubmissions. These calculations used the B3LYP<sup>72-74</sup> global hybrid functional with the LACVP\* basis set, which corresponds to the LANL2DZ<sup>75</sup> effective core potential for transition metals (i.e., Cr, Mn, Fe, Co) and heavier elements (i.e., I or Br) and the 6-31G\* basis for all remaining elements. These geometries were optimized using the L-BFGS algorithm in translation rotation internal coordinates (TRIC)<sup>76</sup> to the default tolerances of  $4.5 \times 10^{-4}$  hartree/bohr for the maximum gradient and  $10^{-6}$  hartree for the energy change between steps. All HS (i.e., quintet) states were calculated with an unrestricted formalism and LS (i.e., singlet) states with a restricted formalism. In all calculations, level shifting of 0.25 Ha was employed between the occupied and virtual spin orbitals. Geometry checks were applied to eliminate optimized structures that deviated from the expected octahedral shape following previously established metrics without modification.<sup>77</sup> Open-shell structures were also removed from the data set following established protocols if the expectation

value of the  $S^2$  operator deviated from its expected value<sup>77</sup> of  $S(S + 1)$  by  $>1 \mu_{\text{B}}^2$  (Supporting Information Table S5).

For optimized TMCs, we followed our established protocol<sup>43</sup> for the calculation of the  $\Delta$ -SCF gap with multiple DFAs using a developer version of Psi4 1.4<sup>78</sup>. We adopted a consistent spin state convention<sup>43</sup>: we removed a majority-spin electron from the  $N$ -electron reference for the  $N-1$ -electron calculation and added a minority-spin electron for the  $N+1$ -electron case. The  $\Delta$ -SCF gap is then computed as  $2 * E[N] - (E[N-1] + E[N+1])$ . In this workflow, the converged wavefunction obtained from the B3LYP geometry optimization was used as an initial guess for the single-point energy calculations with other DFAs, thus maximizing the correspondence of the converged electronic state among all DFAs and also reducing the computational cost. We use 23 DFAs as in our previous work<sup>43</sup> that were chosen to be evenly distributed among the rungs of “Jacob's ladder”<sup>79</sup> (Supporting Information Table S6).

We evaluated the  $r_{\text{ND}}$  diagnostic<sup>61-62, 80</sup> by performing finite-temperature DFT<sup>81</sup> calculations using TeraChem<sup>71</sup>. Specifically, we followed a literature recommendation<sup>61-62, 80</sup> to use a temperature of 9,000 K for B3LYP. Here, we evaluated fractional occupation numbers (FON) from a broadened distribution (i.e., with Fermi–Dirac statistics).

We performed linear response TDDFT calculations with the Tamm-Dancoff approximation using  $\omega$ B97X-D/def2-TZVP followed by the recommendation of a recent benchmark study<sup>82</sup> in Psi4 1.4<sup>78</sup>. We used polarizable continuum implicit solvent model with water ( $\epsilon = 80$ ) as the solvent. Since we focus most on the lowest few excitations, only the first 30 states were computed. We broadened simulated spectra using Lorentzian functions, and we considered only excited states with significant oscillator strength (i.e.,  $f_{\text{osc}} > 0.01$  a.u.).

**ML models.** As in our prior work, we use extended revised autocorrelations<sup>83-84</sup> (eRACs) as descriptors for all our machine learning models. The eRAC features are sums of products and differences of six atom-wise heuristic properties (i.e., topology, identity, electronegativity, covalent radius, nuclear charge, and group number in the periodic table) on the 2D molecular graph. As motivated previously on large TMCs<sup>36</sup>, we applied the maximum bond depth of four and eliminated RACs that were invariant over the mononuclear octahedral transition-metal complexes. We used metal oxidation state and total ligand charge of a complexes as two additional features. Since we would like to discover transition metal chromophores with an LS ground state with certain ranges of  $\Delta$ -SCF gap and  $r_{\text{ND}}$ , we built ML models to predict these three properties. Specifically, we built i) a classification model to predict whether a complex fulfills the consensus LS condition (i.e., > 16 DFAs categorize the ground state to be LS), ii) a regression model to predict  $r_{\text{ND}}$  of a LS complex, and iii) 23 separate models to predict the  $\Delta$ -SCF gap of a LS complex for each DFA (Supporting Information Table S1). In our workflow, we first used the ground state classification model to filter out complexes that do not reach the consensus LS condition. We used the energy from both the HS and LS optimization of a complex as training data for the model to determine its ground spin state. On the contrary, only the LS calculation was used for building the ML models that predict  $\Delta$ -SCF and  $r_{\text{ND}}$ . For the 23  $\Delta$ -SCF gap models, we adopted our established workflow<sup>43</sup> to fine tune the 22 non-B3LYP models initialized by the weights of the B3LYP model to avoid randomness in the weight initialization and to increase the consistency between ANN models trained with DFT data derived from different DFAs.

During each generation during the active learning, we partitioned the data using a random 80%/20% train/test split and used 20% of the training data (i.e., 16% overall) as the validation set.

As in our prior work<sup>36</sup>, all ANN models were trained using Keras<sup>85</sup> with a Tensorflow<sup>86</sup> backend and Hyperopt<sup>87</sup> for hyperparameter selection for gen-0 data (Supporting Information Table S7). For all other generations, the models were only fine-tuned with a reduced learning rate (i.e.,  $10^{-5}$ ) on the combined training set of all previous generations. All ANN models were trained with the Adam optimizer up to 2,000 epochs, and dropout, batch normalization, and early stopping were applied to avoid overfitting.

### **Supporting Information Statement**

Histogram for average ground state spin;  $\Delta$ -SCF gap computed at different DFAs and spin states;  $r_{\text{ND}}$  of optimized structures at LS and HS state; Ground state labeling with DFA consensus and AUC of ML classification models; Comparison of ligands'  $r_{\text{ND}}$ ; Summary first three excited states for complexes that have “dark” states on the Pareto front;  $\Delta$ -SCF gap and  $r_{\text{ND}}$  for functionalized counterpart of complex **F**; Ligands involved in CSD complexes with photo-induced properties; Summary of the filtering statistics during active learning; Summary of 23 DFAs; Range of hyperparameters sampled for ANN models; Data .csv files for all DFT-computed complexes, base complexes with high 2D P[I], and complexes reside in the target zone and Pareto front; Geometries for 812 ligands and DFT-optimized complexes; ML models for  $\Delta$ -SCF gap and  $r_{\text{ND}}$  regression and ground spin state classification.

### **ACKNOWLEDGMENT**

This work was supported by the U.S. Department of Energy, Office of Science, Office of Advanced Scientific Computing, Office of Basic Energy Sciences, via the Scientific Discovery through Advanced Computing (SciDAC) program as well as by the Office of Naval Research

under grant numbers N00014-18-1-2434 and N00014-20-1-2150. C.D. was partially supported by a seed fellowship from the Molecular Sciences Software Institute under NSF grant OAC-1547580. A.N. and D.W.K were partially supported by a National Science Foundation Graduate Research Fellowship under Grants #1122374 and Grant #1745302, respectively. H.J.K. holds a Sloan Fellowship in Chemistry, which supported this work. The authors acknowledge the MIT SuperCloud and Lincoln Laboratory Supercomputing Center for providing HPC resources that have contributed to the research results reported within this paper. The authors thank Adam H. Steeves for providing a critical reading of the manuscript.

## References

1. Shu, Y. N.; Levine, B. G., Simulated Evolution of Fluorophores for Light Emitting Diodes. *J. Chem. Phys.* **2015**, *142* (10), 104104.
2. Gomez-Bombarelli, R.; Aguilera-Iparraguirre, J.; Hirzel, T. D.; Duvenaud, D.; Maclaurin, D.; Blood-Forsythe, M. A.; Chae, H. S.; Einzinger, M.; Ha, D. G.; Wu, T.; Markopoulos, G.; Jeon, S.; Kang, H.; Miyazaki, H.; Numata, M.; Kim, S.; Huang, W. L.; Hong, S. I.; Baldo, M.; Adams, R. P.; Aspuru-Guzik, A., Design of Efficient Molecular Organic Light-Emitting Diodes by a High-Throughput Virtual Screening and Experimental Approach. *Nat. Mater.* **2016**, *15* (10), 1120-+.
3. Kanal, I. Y.; Owens, S. G.; Bechtel, J. S.; Hutchison, G. R., Efficient Computational Screening of Organic Polymer Photovoltaics. *J. Phys. Chem. Lett.* **2013**, *4* (10), 1613-1623.
4. Vogiatzis, K. D.; Polynski, M. V.; Kirkland, J. K.; Townsend, J.; Hashemi, A.; Liu, C.; Pidko, E. A., Computational Approach to Molecular Catalysis by 3d Transition Metals: Challenges and Opportunities. *Chem. Rev.* **2018**, *119*, 2453-2523.
5. Foscatto, M.; Jensen, V. R., Automated in silico Design of Homogeneous Catalysts. *ACS. Catal.* **2020**, *10* (3), 2354-2377.
6. Curtarolo, S.; Hart, G. L.; Nardelli, M. B.; Mingo, N.; Sanvito, S.; Levy, O., The High-Throughput Highway to Computational Materials Design. *Nat. Mater.* **2013**, *12* (3), 191-201.
7. Ong, S. P.; Richards, W. D.; Jain, A.; Hautier, G.; Kocher, M.; Cholia, S.; Gunter, D.; Chevrier, V. L.; Persson, K. A.; Ceder, G., Python Materials Genomics (pymatgen): A Robust, Open-Source Python Library for Materials Analysis. *Comput. Mater. Sci.* **2013**, *68*, 314-319.
8. Nørskov, J. K.; Bligaard, T., The Catalyst Genome. *Angew. Chem. Int. Ed.* **2013**, *52* (3), 776-777.
9. Baiardi, A.; Grimmel, S. A.; Steiner, M.; Türtcher, P. L.; Unsleber, J. P.; Weymuth, T.; Reiher, M., Expansive Quantum Mechanical Exploration of Chemical Reaction Paths. *Acc. Chem. Res.* **2022**, *55* (1), 35-43.
10. Tabor, D. P.; Roch, L. M.; Saikin, S. K.; Kreisbeck, C.; Sheberla, D.; Montoya, J. H.; Dwaraknath, S.; Aykol, M.; Ortiz, C.; Tribukait, H.; Amador-Bedolla, C.; Brabec, C. J.; Maruyama, B.; Persson, K. A.; Aspuru-Guzik, A., Accelerating the discovery of materials for clean energy in the era of smart automation. *Nat. Rev. Mater.* **2018**, *3* (5), 5-20.

11. Borg, C. K. H.; Frey, C.; Moh, J.; Pollock, T. M.; Gorsse, S.; Miracle, D. B.; Senkov, O. N.; Meredig, B.; Saal, J. E., Expanded dataset of mechanical properties and observed phases of multi-principal element alloys. *Sci. Data* **2020**, *7* (1), 430.
12. Kirklin, S.; Saal, J. E.; Meredig, B.; Thompson, A.; Doak, J. W.; Aykol, M.; Rühl, S.; Wolverton, C., The Open Quantum Materials Database (OQMD): assessing the accuracy of DFT formation energies. *npj Comput. Mater.* **2015**, *1* (1), 15010.
13. Meredig, B.; Agrawal, A.; Kirklin, S.; Saal, J. E.; Doak, J.; Thompson, A.; Zhang, K.; Choudhary, A.; Wolverton, C., Combinatorial Screening for New Materials in Unconstrained Composition Space with Machine Learning. *Phys. Rev. B* **2014**, *89* (9), 094104.
14. Dral, P. O., Quantum Chemistry in the Age of Machine Learning. *J. Phys. Chem. Lett.* **2020**, *11* (6), 2336-2347.
15. Butler, K. T.; Davies, D. W.; Cartwright, H.; Isayev, O.; Walsh, A., Machine Learning for Molecular and Materials Science. *Nature* **2018**, *559* (7715), 547-555.
16. Chen, A.; Zhang, X.; Zhou, Z., Machine learning: Accelerating materials development for energy storage and conversion. *InfoMat* **2020**, *2* (3), 553-576.
17. Zhang, L.; Han, J.; Wang, H.; Car, R.; E, W., Deep Potential Molecular Dynamics: A Scalable Model with the Accuracy of Quantum Mechanics. *Phys. Rev. Lett.* **2018**, *120* (14), 143001.
18. Saucedo, H. E.; Gálvez-González, L. E.; Chmiela, S.; Paz-Borbón, L. O.; Müller, K.-R.; Tkatchenko, A., BIGDML—Towards accurate quantum machine learning force fields for materials. *Nat. Commun.* **2022**, *13* (1), 3733.
19. Hermann, J.; Schätzle, Z.; Noé, F., Deep-neural-network solution of the electronic Schrödinger equation. *Nat. Chem.* **2020**, *12* (10), 891-897.
20. Smith, J. S.; Isayev, O.; Roitberg, A. E., ANI-1, A data set of 20 million calculated off-equilibrium conformations for organic molecules. *Sci. Data* **2017**, *4* (1), 170193.
21. Jain, A.; Ong, S. P.; Hautier, G.; Chen, W.; Richards, W. D.; Dacek, S.; Cholia, S.; Gunter, D.; Skinner, D.; Ceder, G.; Persson, K. A., Commentary: The Materials Project: A materials genome approach to accelerating materials innovation. *APL Mater.* **2013**, *1* (1), 011002.
22. Curtarolo, S.; Setyawan, W.; Hart, G. L. W.; Jahnatek, M.; Chepulskii, R. V.; Taylor, R. H.; Wang, S.; Xue, J.; Yang, K.; Levy, O.; Mehl, M. J.; Stokes, H. T.; Demchenko, D. O.; Morgan, D., AFLOW: An automatic framework for high-throughput materials discovery. *Comput. Mater. Sci.* **2012**, *58*, 218-226.
23. Pizzi, G.; Cepellotti, A.; Sabatini, R.; Marzari, N.; Kozinsky, B., AiiDA: automated interactive infrastructure and database for computational science. *Comput. Mater. Sci.* **2016**, *111*, 218-230.
24. Chanussot, L.; Das, A.; Goyal, S.; Lavril, T.; Shuaibi, M.; Riviere, M.; Tran, K.; Heras-Domingo, J.; Ho, C.; Hu, W.; Palizhati, A.; Sriram, A.; Wood, B.; Yoon, J.; Parikh, D.; Zitnick, C. L.; Ulissi, Z., Open Catalyst 2020 (OC20) Dataset and Community Challenges. *ACS. Catal.* **2021**, *11* (10), 6059-6072.
25. Chen, G. a. C., Pengfei and Hsieh, Chang-Yu and Lee, Chee-Kong and Liao, Benben and Liao, Renjie and Liu, Weiwen and Qiu, Jiezhong and Sun, Qiming and Tang, Jie and Zemel, Richard and Zhang, Shengyu In *Alchemy: A Quantum Chemistry Dataset for Benchmarking AI Models*, International Conference on Learning Representations 2019.
26. Jia, H.; Nandy, A.; Liu, M.; Kulik, H. J., Modeling the roles of rigidity and dopants in single-atom methane-to-methanol catalysts. *J. Mater. Chem. A* **2022**, *10* (11), 6193-6203.
27. Janet, J. P.; Duan, C.; Nandy, A.; Liu, F.; Kulik, H. J., Navigating Transition-Metal Chemical Space: Artificial Intelligence for First-Principles Design. *Acc. Chem. Res.* **2021**, *54* (3), 532-545.
28. Walters, W. P.; Murcko, M., Assessing the impact of generative AI on medicinal chemistry. *Nat Biotechnol* **2020**, *38* (2), 143-145.
29. Gomez-Bombarelli, R.; Wei, J. N.; Duvenaud, D.; Hernandez-Lobato, J. M.; Sanchez-Lengeling, B.; Sheberla, D.; Aguilera-Iparraguirre, J.; Hirzel, T. D.; Adams, R. P.; Aspuru-Guzik, A., Automatic Chemical Design Using a Data-Driven Continuous Representation of Molecules. *ACS Cent. Sci.* **2018**, *4* (2), 268-276.

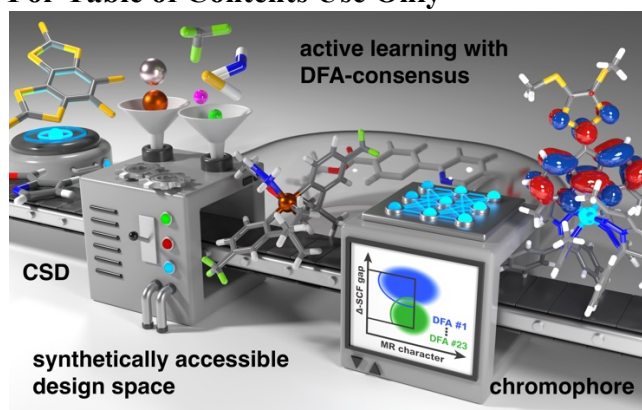
30. Shahriari, B.; Swersky, K.; Wang, Z.; Adams, R. P.; Freitas, N. d., Taking the Human Out of the Loop: A Review of Bayesian Optimization. *Proceedings of the IEEE* **2016**, *104* (1), 148-175.
31. Snoek, J. a. L., Hugo and Adams, Ryan P In *Practical Bayesian Optimization of Machine Learning Algorithms*, Advances in Neural Information Processing Systems, Curran Associates, Inc.: 2012.
32. Bradford, E.; Schweidtmann, A. M.; Lapkin, A., Efficient multiobjective optimization employing Gaussian processes, spectral sampling and a genetic algorithm. *J. Glob. Optim.* **2018**, *71* (2), 407-438.
33. Tallorin, L.; Wang, J.; Kim, W. E.; Sahu, S.; Kosa, N. M.; Yang, P.; Thompson, M.; Gilson, M. K.; Frazier, P. I.; Burkart, M. D.; Gianneschi, N. C., Discovering de novo peptide substrates for enzymes using machine learning. *Nature Communications* **2018**, *9* (1), 5253.
34. Herbol, H. C.; Hu, W.; Frazier, P.; Clancy, P.; Poloczek, M., Efficient search of compositional space for hybrid organic-inorganic perovskites via Bayesian optimization. *npj Comput. Mater.* **2018**, *4* (1), 51.
35. Yuan, R.; Liu, Z.; Balachandran, P. V.; Xue, D.; Zhou, Y.; Ding, X.; Sun, J.; Xue, D.; Lookman, T., Accelerated Discovery of Large Electrostrains in BaTiO<sub>3</sub>-Based Piezoelectrics Using Active Learning. *Adv. Mater.* **2018**, *30* (7), 1702884.
36. Nandy, A.; Duan, C.; Goffinet, C.; Kulik, H. J., New Strategies for Direct Methane-to-Methanol Conversion from Active Learning Exploration of 16 Million Catalysts. *JACS Au* **2022**, *2* (5), 1200-1213.
37. Janet, J. P.; Ramesh, S.; Duan, C.; Kulik, H. J., Accurate Multiobjective Design in a Space of Millions of Transition Metal Complexes with Neural-Network-Driven Efficient Global Optimization. *ACS Cent. Sci.* **2020**, *6* (4), 513-524.
38. Coley, C. W.; Eyke, N. S.; Jensen, K. F., Autonomous Discovery in the Chemical Sciences Part II: Outlook. *Angew. Chem. Int. Ed. Engl.* **2020**, *59* (52), 23414-23436.
39. Gao, W.; Coley, C. W., The Synthesizability of Molecules Proposed by Generative Models. *J. Chem. Inf. Model.* **2020**, *60* (12), 5714-5723.
40. Thakkar, A.; Chadimova, V.; Bjerrum, E. J.; Engkvist, O.; Reymond, J. L., Retrosynthetic accessibility score (RAscore) - rapid machine learned synthesizability classification from AI driven retrosynthetic planning. *Chem. Sci.* **2021**, *12* (9), 3339-3349.
41. Cohen, A. J.; Mori-Sánchez, P.; Yang, W., Challenges for Density Functional Theory. *Chem. Rev.* **2012**, *112* (1), 289-320.
42. Mardirossian, N.; Head-Gordon, M., Thirty years of density functional theory in computational chemistry: an overview and extensive assessment of 200 density functionals. *Mol. Phys.* **2017**, *115* (19), 2315-2372.
43. Duan, C.; Chen, S.; Taylor, M. G.; Liu, F.; Kulik, H. J., Machine learning to tame divergent density functional approximations: a new path to consensus materials design principles. *Chem. Sci.* **2021**, *12* (39), 13021-13036.
44. Duan, C.; Nandy, A.; Kulik, H. J., Machine Learning for the Discovery, Design, and Engineering of Materials. *Annu. Rev. Chem. Biomol. Eng.* **2022**, *13*, 405-429.
45. Janesko, B. G., Replacing Hybrid Density Functional Theory: Motivation and Recent Advances. *Chem. Soc. Rev.* **2021**.
46. Wegeberg, C.; Wenger, O. S., Luminescent First-Row Transition Metal Complexes. *JACS Au* **2021**, *1* (11), 1860-1876.
47. Wenger, O. S., Photoactive Complexes with Earth-Abundant Metals. *J. Am. Chem. Soc.* **2018**, *140* (42), 13522-13533.
48. Ponseca, C. S.; Chábera, P.; Uhlig, J.; Persson, P.; Sundström, V., Ultrafast Electron Dynamics in Solar Energy Conversion. *Chem. Rev.* **2017**, *117* (16), 10940-11024.
49. Yam, V. W.-W.; Au, V. K.-M.; Leung, S. Y.-L., Light-Emitting Self-Assembled Materials Based on d8 and d10 Transition Metal Complexes. *Chem. Rev.* **2015**, *115* (15), 7589-7728.
50. Ardo, S.; Meyer, G. J., Photodriven heterogeneous charge transfer with transition-metal compounds anchored to TiO<sub>2</sub> semiconductor surfaces. *Chem. Soc. Rev.* **2009**, *38* (1), 115-64.

51. Proppe, A. H.; Li, Y. C.; Aspuru-Guzik, A.; Berlinguette, C. P.; Chang, C. J.; Cogdell, R.; Doyle, A. G.; Flick, J.; Gabor, N. M.; van Grondelle, R.; Hammes-Schiffer, S.; Jaffer, S. A.; Kelley, S. O.; Leclerc, M.; Leo, K.; Mallouk, T. E.; Narang, P.; Schlau-Cohen, G. S.; Scholes, G. D.; Vojvodic, A.; Yam, V. W.-W.; Yang, J. Y.; Sargent, E. H., Bioinspiration in light harvesting and catalysis. *Nat. Rev. Mater.* **2020**, *5* (11), 828-846.
52. Kjaer, K. S.; Kaul, N.; Prakash, O.; Chabera, P.; Rosemann, N. W.; Honarfar, A.; Gordivska, O.; Fredin, L. A.; Bergquist, K. E.; Haggstrom, L.; Ericsson, T.; Lindh, L.; Yartsev, A.; Styring, S.; Huang, P.; Uhlig, J.; Bendix, J.; Strand, D.; Sundstrom, V.; Persson, P.; Lomoth, R.; Warnmark, K., Luminescence and reactivity of a charge-transfer excited iron complex with nanosecond lifetime. *Science* **2019**, *363* (6424), 249-253.
53. McCusker, J. K., Electronic structure in the transition metal block and its implications for light harvesting. *Science* **2019**, *363* (6426), 484-488.
54. Braun, J. D.; Lozada, I. B.; Kolodziej, C.; Burda, C.; Newman, K. M. E.; van Lierop, J.; Davis, R. L.; Herbert, D. E., Iron(II) coordination complexes with panchromatic absorption and nanosecond charge-transfer excited state lifetimes. *Nat. Chem.* **2019**, *11* (12), 1144-1150.
55. DiLuzio, S.; Mdluli, V.; Connell, T. U.; Lewis, J.; VanBenschoten, V.; Bernhard, S., High-Throughput Screening and Automated Data-Driven Analysis of the Triplet Photophysical Properties of Structurally Diverse, Heteroleptic Iridium(III) Complexes. *J. Am. Chem. Soc.* **2021**, *143* (2), 1179-1194.
56. Aldrich, K. E.; Fales, B. S.; Singh, A. K.; Staples, R. J.; Levine, B. G.; McCracken, J.; Smith, M. R.; Odom, A. L., Electronic and Structural Comparisons between Iron(II/III) and Ruthenium(II/III) Imide Analogs. *Inorganic Chemistry* **2019**, *58* (17), 11699-11715.
57. Jones, D. R.; Schonlau, M.; Welch, W. J., Efficient Global Optimization of Expensive Black-Box Functions. *J. Glob. Optim.* **1998**, *13* (4), 455-492.
58. Perdew, J. P.; Schmidt, K. In *Jacob's Ladder of Density Functional Approximations for the Exchange-Correlation Energy*, Density Functional Theory and Its Application to Materials, 2001; pp 1-20.
59. Nam, W., Synthetic Mononuclear Nonheme Iron-Oxygen Intermediates. *Acc. Chem. Res.* **2015**, *48* (8), 2415-2423.
60. Duan, C.; Ladera, A. J.; Liu, J. C. L.; Taylor, M. G.; Ariyaratna, I. R.; Kulik, H. J., Exploiting Ligand Additivity for Transferable Machine Learning of Multireference Character across Known Transition Metal Complex Ligands. *J. Chem. Theory Comput.* **2022**.
61. Ramos-Cordoba, E.; Salvador, P.; Matito, E., Separation of dynamic and nondynamic correlation. *Phys. Chem. Chem. Phys.* **2016**, *18* (34), 24015-24023.
62. Ramos-Cordoba, E.; Matito, E., Local Descriptors of Dynamic and Nondynamic Correlation. *J. Chem. Theory Comput.* **2017**, *13* (6), 2705-2711.
63. Kesharwani, M. K.; Sylvetsky, N.; Kohn, A.; Tew, D. P.; Martin, J. M. L., Do CCSD and approximate CCSD-F12 variants converge to the same basis set limits? The case of atomization energies. *J. Chem. Phys.* **2018**, *149* (15), 154109.
64. Ziegler, T.; Rauk, A.; Baerends, E. J., On the Calculation of Multiplet Energies by the Hartree-Fock-Slater Method. *Theoretica chimica acta* **1977**, *43* (3), 261-271.
65. Liu, F.; Duan, C.; Kulik, H. J., Rapid Detection of Strong Correlation with Machine Learning for Transition-Metal Complex High-Throughput Screening. *J. Phys. Chem. Lett.* **2020**, *11* (19), 8067-8076.
66. Fatur, S. M.; Shepard, S. G.; Higgins, R. F.; Shores, M. P.; Damrauer, N. H., A Synthetically Tunable System To Control MLCT Excited-State Lifetimes and Spin States in Iron(II) Polypyridines. *J. Am. Chem. Soc.* **2017**, *139* (12), 4493-4505.
67. Mukherjee, S.; Torres, D. E.; Jakubikova, E., HOMO inversion as a strategy for improving the light-absorption properties of Fe(II) chromophores. *Chem. Sci.* **2017**, *8* (12), 8115-8126.
68. Zhu, Q.-Y.; Lu, W.; Zhang, Y.; Bian, G.-Q.; Gu, J.; Lin, X.-M.; Dai, J., Syntheses, Crystal Structures, and Optical Properties of Metal Complexes with 4',5'-Diaza-9'-(4,5-disubstituted-1,3-dithiol-2-ylidene)fluorene Ligands. *Eur. J. Inorg. Chem.* **2008**, *2008* (2), 230-238.

69. Ioannidis, E. I.; Gani, T. Z. H.; Kulik, H. J., molSimplify: A Toolkit for Automating Discovery in Inorganic Chemistry. *J. Comput. Chem.* **2016**, *37*, 2106-2117.
70. KulikGroup molSimplify documentation. <http://molsimplify.mit.edu> (accessed June 24, 2021).
71. Seritan, S.; Bannwarth, C.; Fales, B. S.; Hohenstein, E. G.; Isborn, C. M.; Kokkila-Schumacher, S. I. L.; Li, X.; Liu, F.; Luehr, N.; Snyder Jr., J. W.; Song, C.; Titov, A. V.; Ufimtsev, I. S.; Wang, L.-P.; Martínez, T. J., TeraChem: A graphical processing unit-accelerated electronic structure package for large-scale ab initio molecular dynamics. *WIREs Comput. Mol. Sci.* **2021**, *11* (2), e1494.
72. Becke, A. D., Density-Functional Thermochemistry. III. The Role of Exact Exchange. *J. Chem. Phys.* **1993**, *98* (7), 5648-5652.
73. Lee, C.; Yang, W.; Parr, R. G., Development of the Colle-Salvetti Correlation-Energy Formula into a Functional of the Electron Density. *Phys. Rev. B* **1988**, *37*, 785--789.
74. Stephens, P. J.; Devlin, F. J.; Chabalowski, C. F.; Frisch, M. J., Ab Initio Calculation of Vibrational Absorption and Circular Dichroism Spectra Using Density Functional Force Fields. *J. Phys. Chem.* **1994**, *98* (45), 11623-11627.
75. Hay, P. J.; Wadt, W. R., Ab Initio Effective Core Potentials for Molecular Calculations. Potentials for the Transition Metal Atoms Sc to Hg. *J. Chem. Phys.* **1985**, *82* (1), 270-283.
76. Wang, L.-P.; Song, C., Geometry optimization made simple with translation and rotation coordinates. *J. Chem. Phys.* **2016**, *144* (21), 214108.
77. Duan, C.; Janet, J. P.; Liu, F.; Nandy, A.; Kulik, H. J., Learning from Failure: Predicting Electronic Structure Calculation Outcomes with Machine Learning Models. *J. Chem. Theory Comput.* **2019**, *15* (4), 2331-2345.
78. Smith, D. G. A.; Burns, L. A.; Simmonett, A. C.; Parrish, R. M.; Schieber, M. C.; Galvelis, R.; Kraus, P.; Kruse, H.; Di Remigio, R.; Alenaizan, A.; James, A. M.; Lehtola, S.; Misiewicz, J. P.; Scheurer, M.; Shaw, R. A.; Schriber, J. B.; Xie, Y.; Glick, Z. L.; Sirianni, D. A.; O'Brien, J. S.; Waldrop, J. M.; Kumar, A.; Hohenstein, E. G.; Pritchard, B. P.; Brooks, B. R.; Schaefer, H. F., 3rd; Sokolov, A. Y.; Patkowski, K.; DePrince, A. E., 3rd; Bozkaya, U.; King, R. A.; Evangelista, F. A.; Turney, J. M.; Crawford, T. D.; Sherrill, C. D., Psi4 1.4: Open-source software for high-throughput quantum chemistry. *J. Chem. Phys.* **2020**, *152* (18), 184108.
79. Perdew, J. P.; Schmidt, K., Jacob's Ladder of Density Functional Approximations for the Exchange-Correlation Energy. *Density Functional Theory and Its Application to Materials* **2001**, *577*, 1-20.
80. Grimme, S.; Hansen, A., A Practicable Real-Space Measure and Visualization of Static Electron-Correlation Effects. *Angew. Chem., Int. Ed.* **2015**, *54* (42), 12308-12313.
81. Weinert, M.; Davenport, J. W., Fractional Occupations and Density-Functional Energies and Forces. *Phys. Rev. B* **1992**, *45* (23), 13709-13712.
82. Liang, J.; Feng, X.; Hait, D.; Head-Gordon, M., Revisiting the Performance of Time-Dependent Density Functional Theory for Electronic Excitations: Assessment of 43 Popular and Recently Developed Functionals from Rungs One to Four. *J. Chem. Theory Comput.* **2022**, *18* (6), 3460-3473.
83. Janet, J. P.; Kulik, H. J., Resolving Transition Metal Chemical Space: Feature Selection for Machine Learning and Structure-Property Relationships. *J. Phys. Chem. A* **2017**, *121* (46), 8939-8954.
84. Harper, D. R.; Nandy, A.; Arunachalam, N.; Duan, C.; Janet, J. P.; Kulik, H. J., Representations and strategies for transferable machine learning improve model performance in chemical discovery. *J. Chem. Phys.* **2022**, *156* (7), 074101.
85. Chollet, F. Keras. <https://keras.io> (accessed June 24, 2021).
86. Abadi, M.; Agarwal, A.; Barham, P.; Brevdo, E.; Chen, Z.; Citro, C.; Corrado, G. S.; Davis, A.; Dean, J.; Devin, M.; Ghemawat, S.; Goodfellow, I.; Harp, A.; Irving, G.; Isard, M.; Jozefowicz, R.; Jia, Y.; Kaiser, L.; Kudlur, M.; Levenberg, J.; Mané, D.; Schuster, M.; Monga, R.; Moore, S.; Murray, D.; Olah, C.; Shlens, J.; Steiner, B.; Sutskever, I.; Talwar, K.; Tucker, P.; Vanhoucke, V.; Vasudevan, V.; Viégas, F.; Vinyals, O.; Warden, P.; Wattenberg, M.; Wicke, M.; Yu, Y.; Zheng, X. *TensorFlow: Large-Scale Machine Learning on Heterogeneous Systems*, 2015.

87. Bergstra, J.; Yamins, D.; Cox, D. D. In *Hyperopt: A Python Library for Optimizing the Hyperparameters of Machine Learning Algorithms*, Proceedings of the 12th Python in science conference, 2013; pp 13-20.

## For Table of Contents Use Only



## Supporting Information for

### Rapid Exploration of a 32.5M Compound Chemical Space with Active Learning to Discover Density Functional Approximation Insensitive and Synthetically Accessible Transitional Metal Chromophores

Chenru Duan<sup>1,2</sup>, Aditya Nandy<sup>1,2</sup>, Gianmarco Terrones<sup>1</sup>, David W. Kastner<sup>1,3</sup>, and Heather J. Kulik<sup>1,2</sup>

<sup>1</sup>Department of Chemical Engineering, Massachusetts Institute of Technology, Cambridge, MA 02139

<sup>2</sup>Department of Chemistry, Massachusetts Institute of Technology, Cambridge, MA 02139

<sup>3</sup>Department of Biological Engineering, Massachusetts Institute of Technology, Cambridge, MA 02139

## Contents

<b>Figure S1</b> Normalized histogram for the average ground state spin	Page S2
<b>Figure S2</b> $\Delta$ -SCF gap computed at HS versus LS optimized geometry	Page S2
<b>Figure S3</b> $\Delta$ -SCF gap computed at BLYP and M06-2X	Page S3
<b>Table S1</b> Ground state labeling with DFA consensus	Page S3
<b>Figure S4</b> $r_{\text{ND}}$ of optimized structures at LS and HS state	Page S3
<b>Figure S5</b> Model AUC for ground spin state classification	Page S4
<b>Figure S6</b> Ligands' $r_{\text{ND}}$ of the 2,432 selected and 1.3M base complexes	Page S4
<b>Table S2</b> Summary first three excited states for the other three complexes	Page S4
<b>Table S3</b> $\Delta$ -SCF gap and $r_{\text{ND}}$ for functionalized counterpart of complex <b>F</b>	Page S5
<b>Table S4</b> Ligands involved in CSD complexes with photo-induced properties	Page S5
<b>Table S5</b> Summary of the filtering statistics for the TMCs at each generation	Page S6
<b>Table S6</b> Summary of 23 DFAs used in this work	Page S7
<b>Table S7</b> Range of hyperparameters sampled for ANN models	Page S8
<b>References</b>	Page S8

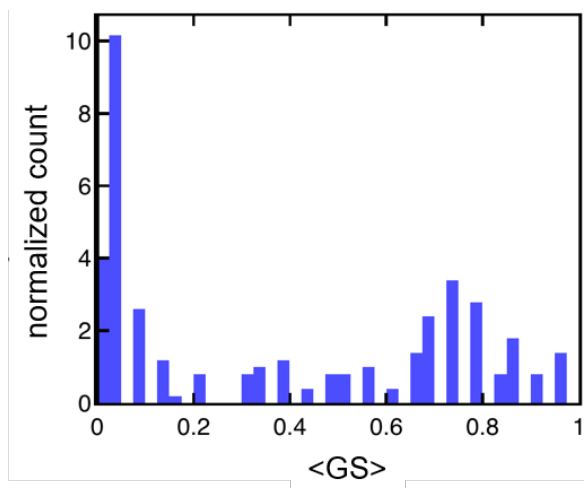


**Figure S1.** Normalized histogram for the average ground state spin ( $\langle GS \rangle$ ) of the gen-0 complexes, with 0 corresponding to the case where all 23 DFAs agree the assignment of LS as the ground state and 1 corresponding to the case where all 23 DFAs agree the assignment of HS as the ground state.

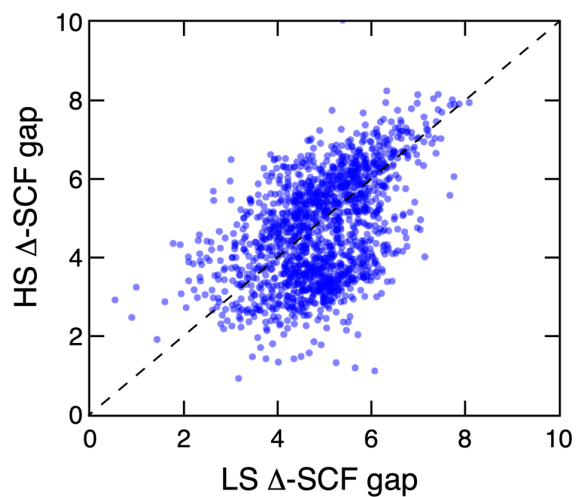


**Figure S2.**  $\Delta$ -SCF gap computed at HS versus LS optimized geometry for the gen-0 complexes computed by B3LYP. The parity is shown as a black dashed line.

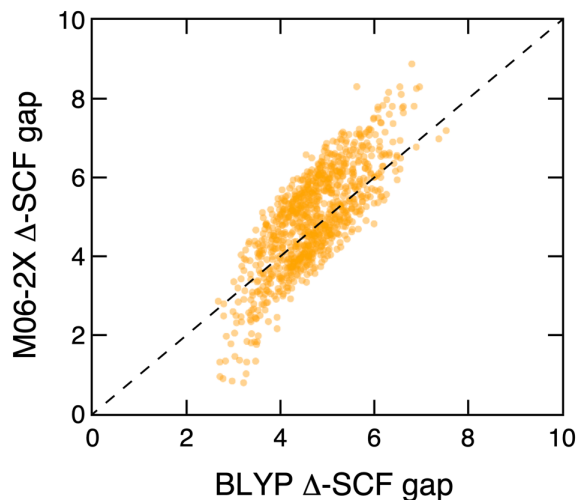


**Figure S3.**  $\Delta$ -SCF gap computed at the LS optimized geometry for the gen-0 complexes computed by BLYP ( $x$  axis) and M06-2X ( $y$  axis). The parity is shown as a black dashed line.

**Table S1.** Ground state (GS) label with respect to the number and percentage of DFAs that determine LS as the GS.

label	number ( $n$ ) of DFAs	percentage ( $p$ ) of DFAs
consensus LS (0)	$n > 16$	$p > 70\%$
no consensus (1)	$16 \geq n > 6$	$70\% \geq p > 30\%$
consensus HS (2)	$n \leq 6$	$p \leq 30\%$

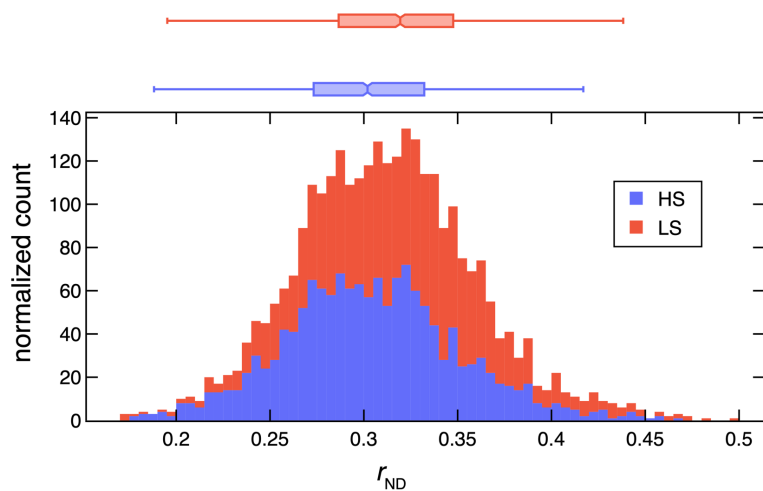


**Figure S4.** Normalized stacked histogram for  $r_{\text{ND}}$  of optimized structures at LS (red) and HS (blue) state for gen-0 complexes with boxes indicating their mean and standard deviations on the top margin.

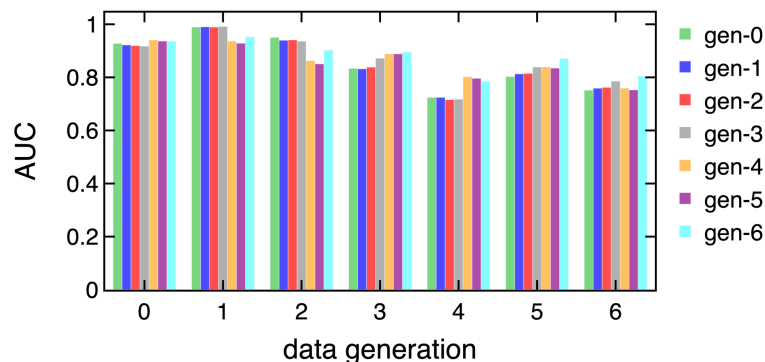


**Figure S5.** Model AUC for ground spin state classification from gen-0 to gen-6. At each generation, the ML models are trained on the combined training set of all previous generations and are tested on the set-aside test set of each generation separately. Since the number of complexes in each class and generation is small (after gen-0), the relative AUC of different models within each data generation is more meaningful than the comparisons of AUC from different data generations.

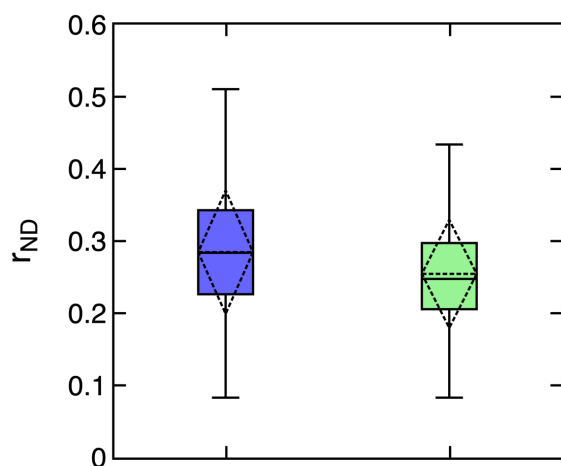


**Figure S6.** Box plot for ligands'  $r_{\text{ND}}$  of the 2,432 complexes with 2D PI > 1/6 evaluated by gen-3 ML models (green) and the 1.3M base complexes (blue). For each box, the median is shown as a horizontal solid line, the mean and std. dev. are shown as a dashed diamond, and the two extrema are shown by the vertical bar.

**Table S2.** Summary of the properties for the first three excited states for the three complexes that lie on the Pareto front but do not have desired excited state properties.

$\Delta$ -SCF gap	$r_{\text{ND}}$	1 <sup>st</sup> excited state		2 <sup>nd</sup> excited state		3 <sup>rd</sup> excited state	
		energy (eV)	$f_{\text{osc}}$ (a.u.)	energy (eV)	$f_{\text{osc}}$ (a.u.)	energy (eV)	$f_{\text{osc}}$ (a.u.)
3.40	0.256	2.50	0.001	2.57	0.001	2.64	0.000
2.48	0.299	2.43	0.001	2.48	0.002	2.56	0.002
3.01	0.269	2.28	0.000	2.50	0.000	2.51	0.000

**Table S3.** Summary of  $\Delta$ -SCF gap and  $r_{ND}$  for the other functionalized counterpart of complex **F** in the main text. The use of "--" corresponds to the case with no functionalization. Complex **F** is shaded in blue.

depth ( <i>d</i> )	functional group	$\Delta$ -SCF gap	$r_{ND}$
--	--	2.82	0.301
<b>3</b>	CH <sub>3</sub>	<b>2.38</b>	<b>0.306</b>
4	CH <sub>3</sub>	3.04	0.288
4	NH <sub>2</sub>	3.17	0.309
5	Cl <sup>-</sup>	3.14	0.301
5	F <sup>-</sup>	2.81	0.302

**Table S4.** Summary of ligands in complexes **A-F** that have parent complexes in CSD that demonstrate interesting photo-induced properties and their references. The complex ID corresponds to the index of the six complexes in Figure 6 of the main text. The ligand ID is our internal database ID, for which the corresponding geometry can be found in the Supporting Information Data. For each ligand, the refcode for the CSD complex that contains this ligand and demonstrates interesting photo-induced properties is also shown.

complex ID	ligand ID	ligand chemical name	CSD refcode	relevant property and reference
<b>F</b>	5fad527635c34d073da22057	4',5'-diaz-9'-[4,5-bis(methylthio)-1,3-dithiol-2-ylidene]fluorene	MIVSIU	nonlinear optical property <sup>1</sup>
<b>E</b>	5fad60c035c34d073da31750	2-(2,6-dichlorophenyl)-1H-imidazo[4,5-f][1,10]phenanthroline	ROVSEC	peak of UV-vis spectra in the visible light region <sup>2</sup>
<b>D</b>	5fad528035c34d073da22500	1,2-bis(dimethylphosphino)ethane	JUWKOD	luminescence <sup>3</sup>
<b>A, C, D</b>	5fad542a35c34d073da26ae3	Bis(1-methylimidazol-2-yl)-(4-methoxyphen-1-yl)methanol	EWAEAE	peak of UV-vis spectra in the visible light region <sup>4</sup>
<b>B</b>	5fad67af35c34d073da3526f	1,2-bis(phosphorinan-1-yl)ethane	XAZZED	photochemically induced oxidation <sup>5</sup>

**Table S5.** Summary of the filtering statistics for the TMCs at each generation, including the number attempted, number of complexes with valid initial geometry (i.e., no ligand clashing), and the number of complexes have good geometry and  $\langle S^2 \rangle$  (judged by our established protocols<sup>6-7</sup>) after converged geometry optimizations. Generations that explored the base complexes space are shade in blue and those explored the functionalized complexes are shaded in green.

generation	attempted	valid initial geometry	converged, good geometry and $\langle S^2 \rangle$
0	2000	1822	1470
1	200	188	146
2	200	195	157
3	200	188	146
4	200	143	91
5	200	184	151
6	200	188	150

**Table S6.** Summary of 23 DFAs in the original work of Duan *et al.*<sup>8</sup>, including the rungs on “Jacob’s ladder” of DFT, HF exchange fraction, LRC range-separation parameter (bohr<sup>-1</sup>), MP2 correlation fraction, and whether empirical (i.e., D3) dispersion correction is included.

DFA	type	exchange type	HF exchange percentage	LRC parameter (bohr <sup>-1</sup> )	RS	MP2 correlation	D3 dispersion
BP86 <sup>9-10</sup>	GGA	GGA	--	--	--	--	no
BLYP <sup>11-12</sup>	GGA	GGA	--	--	--	--	no
PBE <sup>13</sup>	GGA	GGA	--	--	--	--	no
TPSS <sup>14</sup>	meta-GGA	meta-GGA	--	--	--	--	no
SCAN <sup>15</sup>	meta-GGA	meta-GGA	--	--	--	--	no
M06-L <sup>16</sup>	meta-GGA	meta-GGA	--	--	--	--	no
MN15-L <sup>17</sup>	meta-GGA	meta-GGA	--	--	--	--	no
B3LYP <sup>18-20</sup>	GGA hybrid	GGA	0.200	--	--	--	no
B3P86 <sup>9, 18</sup>	GGA hybrid	GGA	0.200	--	--	--	no
B3PW91 <sup>18, 21</sup>	GGA hybrid	GGA	0.200	--	--	--	no
PBE0 <sup>22</sup>	GGA hybrid	GGA	0.250	--	--	--	no
$\omega$ B97X <sup>23</sup>	RS hybrid	GGA	0.158	0.300	--	--	no
LRC- $\omega$ PBEh <sup>24</sup>	RS hybrid	GGA	0.200	0.200	--	--	no
TPSSH <sup>14</sup>	meta-GGA hybrid	meta-GGA	0.100	--	--	--	no
SCAN0 <sup>25</sup>	meta-GGA hybrid	meta-GGA	0.250	--	--	--	no
M06 <sup>26</sup>	meta-GGA hybrid	meta-GGA	0.270	--	--	--	no
M06-2X <sup>26</sup>	meta-GGA hybrid	meta-GGA	0.540	--	--	--	no
MN15 <sup>27</sup>	meta-GGA hybrid	meta-GGA	0.440	--	--	--	no
B2GP-PLYP <sup>28</sup>	double hybrid	GGA	0.650	--	--	0.360	no
PBE0-DH <sup>29</sup>	double hybrid	GGA	0.500	--	--	0.125	no
DSD-BLYP-D3BJ <sup>30</sup>	double hybrid	GGA	0.710	--	--	1.000	yes
DSD-PBEB95-D3BJ <sup>30</sup>	double hybrid	GGA	0.660	--	--	1.000	yes
DSD-PBEP6-D3BJ <sup>30</sup>	double hybrid	GGA	0.690	--	--	1.000	yes

**Table S7.** Range of hyperparameters sampled for ANN models trained from scratch with Hyperopt<sup>31</sup>. The lists in the architecture row can refer to one, two, or three hidden layers (i.e., the number of items in the list), and the number of nodes in each layer are denoted as elements of the list. The built-in Tree of Parzen Estimator algorithm in Hyperopt was used for the hyperparameter selection process.

Architecture	[[128], [256], [512], [128, 128], [256, 256], [512, 512], [128, 128, 128], [256, 256, 256], [512, 512, 512]]
L2 regularization	[1e-6, 1]
Dropout rate	[0, 0.5]
Learning rate	[1e-6, 1e-3]
Beta1	[0.75, 0.99]
Batch size	[16, 32, 64, 128, 256, 512]

## References

- Zhu, Q.-Y.; Lu, W.; Zhang, Y.; Bian, G.-Q.; Gu, J.; Lin, X.-M.; Dai, J., Syntheses, Crystal Structures, and Optical Properties of Metal Complexes with 4',5'-Diaza-9'-(4,5-disubstituted-1,3-dithiol-2-ylidene)fluorene Ligands. *Eur. J. Inorg. Chem.* **2008**, 2008 (2), 230-238.
- Wang, Y.; Zhang, Y.; Zhu, D.; Ma, K.; Ni, H.; Tang, G., Synthesis, structural characterization and theoretical approach of the tri(2-(2,6-dichlorophenyl)-1H-imidazo[4,5-f][1,10]phenanthroline) cobalt(II). *Spectrochimica Acta Part A: Molecular and Biomolecular Spectroscopy* **2015**, 147, 31-42.
- Groué, A.; Tranchier, J. P.; Rager, M. N.; Gontard, G.; Métivier, R.; Buriez, O.; Khatyr, A.; Knorr, M.; Amouri, H., Cyclometalated Rhodium and Iridium Complexes Containing Masked Catecholates: Synthesis, Structure, Electrochemistry, and Luminescence Properties. *Inorganic Chemistry* **2022**, 61 (12), 4909-4918.
- Pursche, D.; Triller, M. U.; Slinn, C.; Reddig, N.; Rompel, A.; Krebs, B., Mimicking the reduced, oxidized and azide inhibited form of manganese superoxide dismutase by mononuclear Mn compounds utilizing tridentate ligands. *Inorganica Chimica Acta* **2004**, 357 (6), 1695-1702.
- Field, L. D.; Thomas, I. P.; Turner, P.; Hambley, T. W., Synthesis and Crystal Structures of [Fe(bpe6)<sub>2</sub>Cl<sub>2</sub>] and [Fe(bpe6)<sub>2</sub>Cl<sub>2</sub>]<sup>+</sup> [FeCl<sub>4</sub>]<sup>-</sup> (bpe6 = 1,2-Bis(phosphorinan-1-yl)ethane). *Australian Journal of Chemistry* **2000**, 53 (7), 541-544.
- Nandy, A.; Duan, C.; Janet, J. P.; Gugler, S.; Kulik, H. J., Strategies and Software for Machine Learning Accelerated Discovery in Transition Metal Chemistry. *Industrial & Engineering Chemistry Research* **2018**, 57 (42), 13973-13986.
- Duan, C.; Janet, J. P.; Liu, F.; Nandy, A.; Kulik, H. J., Learning from Failure: Predicting Electronic Structure Calculation Outcomes with Machine Learning Models. *Journal of Chemical Theory and Computation* **2019**, 15 (4), 2331-2345.
- Duan, C.; Chen, S.; Taylor, M. G.; Liu, F.; Kulik, H. J., Machine learning to tame divergent density functional approximations: a new path to consensus materials design principles. *Chem. Sci.* **2021**, 12 (39), 13021-13036.
- Perdew, J. P., Density-Functional Approximation for the Correlation-Energy of the Inhomogeneous Electron-Gas. *Phys. Rev. B* **1986**, 33 (12), 8822-8824.

10. Becke, A. D., Density-Functional Exchange-Energy Approximation with Correct Asymptotic-Behavior. *Physical Review A* **1988**, *38* (6), 3098-3100.
11. Devlin, F. J.; Finley, J. W.; Stephens, P. J.; Frisch, M. J., Ab-Initio Calculation of Vibrational Absorption and Circular-Dichroism Spectra Using Density-Functional Force-Fields - a Comparison of Local, Nonlocal, and Hybrid Density Functionals. *Journal of Physical Chemistry* **1995**, *99* (46), 16883-16902.
12. Miehlich, B.; Savin, A.; Stoll, H.; Preuss, H., Results Obtained with the Correlation-Energy Density Functionals of Becke and Lee, Yang and Parr. *Chemical Physics Letters* **1989**, *157* (3), 200-206.
13. Perdew, J. P.; Burke, K.; Ernzerhof, M., Generalized Gradient Approximation Made Simple. *Phys. Rev. Lett.* **1996**, *77* (18), 3865-3868.
14. Tao, J. M.; Perdew, J. P.; Staroverov, V. N.; Scuseria, G. E., Climbing the Density Functional Ladder: Nonempirical Meta-Generalized Gradient Approximation Designed for Molecules and Solids. *Phys. Rev. Lett.* **2003**, *91* (14), 146401.
15. Sun, J. W.; Ruzsinszky, A.; Perdew, J. P., Strongly Constrained and Appropriately Normed Semilocal Density Functional. *Phys. Rev. Lett.* **2015**, *115* (3), 036402.
16. Zhao, Y.; Truhlar, D. G., A New Local Density Functional for Main-Group Thermochemistry, Transition Metal Bonding, Thermochemical Kinetics, and Noncovalent Interactions. *J. Chem. Phys.* **2006**, *125* (19), 194101.
17. Yu, H. S.; He, X.; Truhlar, D. G., MN15-L: A New Local Exchange-Correlation Functional for Kohn-Sham Density Functional Theory with Broad Accuracy for Atoms, Molecules, and Solids. *J. Chem. Theory Comput.* **2016**, *12* (3), 1280-1293.
18. Becke, A. D., Density-Functional Thermochemistry. III. The Role of Exact Exchange. *J. Chem. Phys.* **1993**, *98* (7), 5648-5652.
19. Lee, C.; Yang, W.; Parr, R. G., Development of the Colle-Salvetti Correlation-Energy Formula into a Functional of the Electron Density. *Phys. Rev. B* **1988**, *37*, 785--789.
20. Stephens, P. J.; Devlin, F. J.; Chabalowski, C. F.; Frisch, M. J., Ab Initio Calculation of Vibrational Absorption and Circular Dichroism Spectra Using Density Functional Force Fields. *J. Phys. Chem.* **1994**, *98* (45), 11623-11627.
21. Perdew, J. P.; Chevary, J. A.; Vosko, S. H.; Jackson, K. A.; Pederson, M. R.; Singh, D. J.; Fiolhais, C., Atoms, Molecules, Solids, and Surfaces - Applications of the Generalized Gradient Approximation for Exchange and Correlation. *Phys. Rev. B* **1992**, *46* (11), 6671-6687.
22. Adamo, C.; Barone, V., Toward Reliable Density Functional Methods Without Adjustable Parameters: The PBE0 Model. *J. Chem. Phys.* **1999**, *110* (13), 6158-6170.
23. Chai, J. D.; Head-Gordon, M., Systematic Optimization of Long-Range Corrected Hybrid Density Functionals. *J. Chem. Phys.* **2008**, *128* (8), 084106.
24. Rohrdanz, M. A.; Martins, K. M.; Herbert, J. M., A Long-Range-Corrected Density Functional That Performs Well for Both Ground-State Properties and Time-Dependent Density Functional Theory Excitation Energies, Including Charge-Transfer Excited States. *J. Chem. Phys.* **2009**, *130* (5), 054112.
25. Hui, K.; Chai, J. D., SCAN-based Hybrid and Double-Hybrid Density Functionals From Models Without Fitted Parameters. *J. Chem. Phys.* **2016**, *144* (4), 044114.
26. Zhao, Y.; Truhlar, D. G., The M06 Suite of Density Functionals for Main Group Thermochemistry, Thermochemical Kinetics, Noncovalent Interactions, Excited States, and Transition Elements: Two New Functionals and Systematic Testing of Four M06-Class

- Functionals and 12 Other Functionals. *Theoretical Chemistry Accounts* **2008**, *120* (1-3), 215-241.
27. Yu, H. Y. S.; He, X.; Li, S. H. L.; Truhlar, D. G., MN15: A Kohn-Sham Global-Hybrid Exchange-Correlation Density Functional With Broad Accuracy for Multi-Reference and Single-Reference Systems and Noncovalent Interactions. *Chem. Sci.* **2016**, *7* (9), 6278-6279.
28. Karton, A.; Tarnopolsky, A.; Lamere, J. F.; Schatz, G. C.; Martin, J. M. L., Highly Accurate First-Principles Benchmark Data Sets for the Parametrization and Validation of Density Functional and Other Approximate Methods. Derivation of a Robust, Generally Applicable, Double-Hybrid Functional for Thermochemistry and Thermochemical Kinetics. *Journal of Physical Chemistry A* **2008**, *112* (50), 12868-12886.
29. Bremond, E.; Adamo, C., Seeking for Parameter-Free Double-Hybrid Functionals: The PBE0-DH Model. *J. Chem. Phys.* **2011**, *135* (2), 024106.
30. Kozuch, S.; Martin, J. M. L., Spin-Component-Scaled Double Hybrids: An Extensive Search for the Best Fifth-Rung Functionals Blending DFT and Perturbation Theory. *Journal of Computational Chemistry* **2013**, *34* (27), 2327-2344.
31. Bergstra, J.; Yamins, D.; Cox, D. D. In *Hyperopt: A Python Library for Optimizing the Hyperparameters of Machine Learning Algorithms*, Proceedings of the 12th Python in science conference, 2013; pp 13-20.